JOURNAL OF Materials CHEMISTRY

Preparation, structural, electrical and magnetic properties of tetrathiafulvalene†-Au(pds)$_2$ salts (pds = pyrazine-2,3-diselenolate)

Jorge Morgado,[a,b] Isabel C. Santos,[b] Luís F. Veiros,[a] César Rodrigues,[a] Rui T. Henriques,[a,b] M. Teresa Duarte,[a] Luís Alcácer[a] and Manuel Almeida*[b]

[a]*Dep. Eng. Química, Instituto Superior Técnico, Av. Rovisco Pais, P-1049-001 Lisboa, Portugal*
[b]*Dep. Química, Instituto Tecnológico e Nuclear, P-2686-953 Sacavém, Portugal. E-mail: malmeida@itn.pt*

Received 8th March 2001, Accepted 22nd May 2001
First published as an Advance Article on the web 27th June 2001

The combination of the electron donor tetrathiafulvalene, ttf, with the gold complex bis(pyrazine-2,3-diselenolate)aurate(III), Au(pds)$_2^-$, afforded three different compounds depending on the preparative conditions: (ttf)$_2$[Au(pds)$_2$]$_2$ (**1**), (ttf)$_3$[Au(pds)$_2$]$_2$ (**2**) and (ttf)$_3$[Au(pds)$_2$]$_3$ (**3**). Compound **1** was obtained by interdiffusion of (ttf)$_3$(BF$_4$)$_2$ and (NBu$^n_4$)Au(pds)$_2$ in acetonitrile. Compounds **2** and **3** were obtained by electrocrystallisation from ttf and (NBu$^n_4$)Au(pds)$_2$ solutions in dichloromethane and acetonitrile respectively. These compounds were characterised by X-ray diffraction and electrical and magnetic studies. In the crystal structure of compound **1** are two types of ttf motifs; dimers and isolated units. In the structures of compounds **2** and **3** the ttf units are arranged in trimers. In compound **2** the ttf units form trimerised segregated stacks separated by Au(pds)$_2$ units with their long axis almost parallel to the stacking axis. In **3** each ttf trimer is surrounded by a cage of four Au(pds)$_2$ units, and is arranged perpendicularly to the nearest neighbouring trimers. Compounds **1** and **2** exhibit a semiconducting behaviour with room temperature conductivities of 10^{-4} S cm^{-1} and 10^{-2} S cm^{-1}, respectively. Compound **2** is essentially diamagnetic, while compound **1** shows a large paramagnetic susceptibility, at room temperature $\chi_p = 13 \times 10^{-4}$ emu mol^{-1}, following a Curie–Weiss law above 50 K. Compound **3** is paramagnetic with a temperature independent EPR signal in the range 100–300 K.

1. Introduction

Square planar transition metal bisdithiolate complexes are widely used in the preparation of molecular conductors.[1] In some cases these complexes can form in solid-state stacks or bidimensional networks of partially oxidised species that are responsible for metallic[2] or even superconducting properties.[1c,1d,3] In other cases they are in a monoanionic form, and act as a simple counter ion without playing a significant role in the electron transport properties which are assured by electron donor species. For example, in the perylene based organic conductors, extensively studied in our laboratory,[1b,4] the stabilisation of the partially oxidised perylene chains responsible for metallic conduction as (Per)$_2^+$ is achieved by the M(mnt)$_2^-$ anions (mnt = maleonitrile dithiolate). In such cases the metal complex anions depending on the metal can be diamagnetic or paramagnetic, thus offering the possibility of studying the interaction between localised magnetic moments and conduction electrons.

The combination of one donor with one acceptor to form charge transfer salts leading to solids with more than one stoichiometry and even to different structures (polymorphs) of the same composition is not uncommon. One example is given by bis(ethylenedithio)tetrathiafulvalene or bedt-ttf, probably the most widely used electron-donor in the preparation of organic superconductors, bedt-ttf with different anions makes salts in many different phases, not always correlated with the preparative conditions.[5]

In our research group we are interested in square planar transition metal bisdichalcogenate complexes with ligands bearing electronegative atoms which are able to stabilise high oxidation states of the transition metal. In this paper we report on the use of the pyrazine-2,3-diselenolate ligand, pds^{2-}, to synthesise the gold(III) complex [Au(pds)$_2$]$^-$. By combination of this complex with the electron-donor tetrathiafulvalene, ttf, we have isolated three different compounds: (ttf)$_2$[Au(pds)$_2$]$_2$, (**1**), (ttf)$_3$[Au(pds)$_2$]$_2$, (**2**), and (ttf)$_3$[Au(pds)$_2$]$_3$, (**3**). The fully ionic compounds **1** and **3** were obtained from acetonitrile solutions by interdiffusion of (ttf)$_3$(BF$_4$)$_2$ and (NBu$^n_4$)Au(pds)$_2$ and by electrocrystallisation respectively, while the mixed valence compound (**2**) was obtained by electrocrystallisation from solutions in the less polar dichloromethane. A preliminary report on the properties of the compounds **2** and **3** was previously presented.[6] In this paper we present a more complete study of the properties of these three compounds, encompassing the structure solved by X-ray diffraction, molecular orbital calculations, and measurements of magnetic and electrical transport properties.

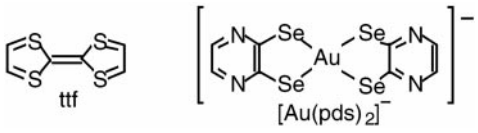

2. Experimental

2.1. Synthesis

The pds$_2^-$ ligand was synthesised as the sodium salt, Na$_2$(pds), following the previously reported procedure for the preparation of the sulfur analogue.[7] The gold complex was prepared in water by reaction of Na$_2$(pds) with KAuCl$_4$ and precipitated as

†Tetrathiafulvalene = 2-(1′,3′-dithiol-2′-ylidene)-1,3-dithiole.

 DOI: 10.1039/b102220m

the tetrabutylammonium salt, $(NBu^n_4)Au(pds)_2$, by addition of tetrabutylammonium chloride. The product was recrystallised from acetone–hexane. ttf was purchased from EGA-Chemie, and purified by gradient sublimation. $(ttf)_3(BF_4)_2$ was prepared according to ref. 8.

$(ttf)_2[Au(pds)_2]_2$ (**1**) as long needle shaped dark crystals, typically $10\times0.8\times0.7\ mm^3$, was prepared by a diffusion-controlled reaction between $(ttf)_3(BF_4)_2$ and $(NBu^n_4)Au(pds)_2$ in acetonitrile, in a H-shaped cell (Found: C, 19.41; H, 0.82; N, 6.09; S, 14.51. $C_{28}H_{16}N_8S_8Se_8Au_2$ requires C, 19.26; H, 0.92; N, 6.42; S, 14.68%). By an electrocrystallisation method, using solutions of ttf ($\approx1.7\ mmol\ l^{-1}$) and $(NBu^n_4)[Au(pds)_2]$ ($\approx0.85\ mmol\ l^{-1}$), under galvanostatic conditions (current density $\approx2\ \mu A\ cm^{-2}$), two different compounds were obtained, on platinum electrodes after a few days, depending on the solvent used: $(ttf)_3[Au(pds)_2]_2$ (**2**) was isolated from dichloromethane solutions as dark thin crystals with dimensions up to $2\times1\times0.05\ mm^3$ (Found: C, 20.6; H, 1.0; N, 5.51. $C_{34}H_{20}N_8S_{12}Se_8Au_2$ requires C, 20.93; H, 1.03; N, 5.74%) while acetonitrile solutions afforded $(ttf)_3[Au(pds)_2]_3$ (**3**) as very small (up to $\sim1\times0.5\times0.1\ mm^3$) dark crystals (Found: C, 19.58; H, 0.74; N, 6.44. $C_{42}H_{24}N_{12}S_{12}Se_{12}Au_3$ requires C, 19.26; H, 0.92; N, 6.42%)

2.2. X-Ray structure determination‡

Crystals of the three compounds were mounted in a goniometer head. X-Ray data were collected at room temperature on an Enraf-Nonius CAD4 diffractometer using graphite monochromatised Mo-Kα radiation ($\lambda=0.71069$ Å) in the ω-2θ scan mode. The same experimental procedure was used to determine the X-ray structure of the three compounds as follows. Accurate cell dimensions were obtained using 25 reflections. The crystal orientation, refinement of cell parameters and intensity measurements were carried out using the program CAD4.[9] Intensities were corrected for Lorentz polarisation effects and for absorption by an empirical method based on ψ-scan data. The structures were solved by Patterson methods using the program SHELXS86[10] and completed by Fourier difference techniques and refined by least-squares methods using the program SHELXL97.[11] All non-hydrogen atoms were refined anisotropically. Hydrogen atoms were placed in calculated positions. Molecular and crystal graphics were prepared with programs ORTEPIII[12] and SCHAKAL-97.[13]‡

2.3. Molecular orbital calculations

The molecular orbital calculations were made using the extended Hückel method[14] with modified H_{ij} values.[15] The band structure calculations were performed with the tight-binding approach of Hückel method.[16] The s and p orbitals were described by single Slater-type wave functions, and only s and p orbitals were considered for S. Three-dimensional representations of orbitals were drawn using the program CACAO.[17]

The calculations for the ttf stacks of compound **2** were performed on the real structures. Calculations were also performed on a model ttf trimer, based on the real structures, resulting from the eclipsed stacking of three planar ttf units, with an interplanar distance between adjacent units of 3.55 Å. The following distances (Å) were used: C–C 1.35; C–S 1.73 and C–H 1.08.

2.4. Magnetic and electrical properties

Static magnetic susceptibility measurements, in the temperature range 4–300 K, were performed using a Faraday system (Oxford Instruments) equipped with a 7 T superconducting magnet. The magnetisation measurements were performed under a static magnetic field of 3.5 T for $(ttf)_2[Au(pds)_2]_2$ (**1**) and of 2 T for $(ttf)_3[Au(pds)_2]_2$ (**2**). The force on the polycrystalline samples, contained in a previously measured thin-walled Teflon bucket, was measured with a microbalance (Sartorius S3D-V) applying forward and reverse gradients of $5\ T\ m^{-1}$. The paramagnetic susceptibility was calculated considering a diamagnetic correction estimated from tabulated Pascal constants.

EPR spectra were obtained in a conventional X-band spectrometer (Bruker ESP 300 E), equipped with a microwave bridge ER041XK, a rectangular cavity operating in T102 mode, a field controller ER 032M system and a Oxford ESR-900 cryostat, which enabled measurements in the temperature range 4–300 K and the temperature was monitored by a Au(0.07 at.% Fe)-chromel thermocouple placed close to the sample. The measurements were performed on either single crystals or polycrystalline samples, placed inside a quartz tube. The modulation amplitude was kept well below the line width and the microwave power well below saturation.

The electrical resistivity and thermoelectric power were measured along the longer axis of the same crystal, placed in a cell attached to the cold stage of a closed-cycle helium refrigerator with accessible temperature in the range 16–310 K. In a first step, the thermoelectric power was measured using a slow a.c. technique[18] in an apparatus similar to that described by Chaikin and Kwak.[19] The thermal gradients were kept below 1 K and monitored by a Au(0.07 at.% Fe)-chromel thermocouple measured with a Keithley 181 nanovoltmeter. A similar thermocouple was used to measure the temperature of the sample. The extremities of the sample were directly glued to the $\phi=25\ \mu m$ gold wires (Goodfellow, 99.99% pure) with platinum paint (Demetron 308A). The thermoelectric voltage was measured with a Keithley 181 nanovoltmeter and the absolute thermopower was calculated after correction for the absolute thermopower of gold using the data of Huebner.[20] In a second step the electrical resistance was measured with the four-in line configuration by placing two extra contacts in the sample. For low impedance samples of $(ttf)_3[Au(pds)_2]_2$ (**2**) we used a low-frequency (77 Hz) 1 μA current and the voltage drop across the inner contacts was measured with a lock-in amplifier (EG&G PAR Model 5301). For the samples of $(ttf)_2[Au(pds)_2]_2$ (**1**) with higher resistance, a d.c. method was used, the electrical resistance being measured by application of direct and reverse current of 1 μA between the two outer contacts with a Keithley 224 current source and taking the average of the absolute voltage drop measured at the inner contacts with a Keithley 619 electrometer.

3. Results and discussion

3.1. Crystal structure

$(ttf)_2[Au(pds)_2]_2$, (1). This compound crystallises in the triclinic system, space group $P\bar{1}$, with the unit cell parameters given in Table 1. The asymmetric unit contains two independent ttf units and two $Au(pds)_2$ units, the numbering scheme is shown in Fig. 1. The ttf units are found either as isolated (ttf(2)) or as dimers (ttf(1)) inside a cage formed by four $Au(pds)_2$ units.

The ttf units are almost planar. The rms deviations of the atoms from the average plane are 0.0454 Å in ttf(1) and 0.0581 Å in ttf(2). The ttf dimers are formed by a nearly eclipsed overlap of ttf(1) units, related by an inversion centre, at an interplanar distance of 3.50(3) Å.

The $Au(pds)_2$ complex is expected to be planar. However we found significant deviations from planarity. In the $Au(1)(pds)_2$ unit, the two pyrazine rings present a small boat distortion. The central plane defined by Au1Se1Se2Se3Se4

‡CCDC reference numbers 159179–159181. See http://www.rsc.org/suppdata/jm/b1/b102220m/ for crystallographic files in .cif or other electronic format.

Table 1 Crystal data and structure refinement of $(ttf)_2[Au(pds)_2]_2$ (**1**), $(ttf)_3[Au(pds)_2]_2$(**2**) and $(ttf)_3[Au(pds)_2]_3$(**3**)

	$(ttf)_2[Au(pds)_2]_2$ (**1**)	$(ttf)_3[Au(pds)_2]_2$(**2**)	$(ttf)_3[Au(pds)_2]_3$(**3**)
Empirical formula	C_{28} H_{16} N_8 S_8 Se_8 Au_2	C_{34} H_{20} N_8 S_{12} Se_8 Au_2	C_{42} H_{24} N_{12} S_{12} Se_{12} Au_3
Formula weight	1746.58	1950.92	2619.88
Crystal system	Triclinic	Monoclinic	Monoclinic
Space group	$P\bar{1}$	$C2/m$	$P2_1/n$
a/Å	9.2248(15)	22.437(9)	9.775(2)
b/Å	14.095(2)	10.981(1)	20.404(2)
c/Å	17.050(2)	10.854(5)	15.424(2)
α/°	92.524(10)		
β/°	105.622(9)	91.79(2)	95.25(2)
γ/°	101.521(9)		
V/Å^3	2080.8(6)	2672.9(2)	3063.4(8)
Z	2	2	2
D_c/Mg m^{-3}	2.788	2.424	2.840
μ/mm^{-1}	14.477	11.435	14.751
Reflections collected	10351	3807	6311
Independent reflections	10019 [R(int) = 0.0604]	3392 [R(int) = 0.0461]	5953 [R(int) = 0.0315]
Goodness-of-fit on F^2	1.113	0.907	1.129
Final R indices [$I > 2\sigma(I)$]	$R = 0.0714$	$R = 0.0554$	$R = 0.0682$
	w$R = 0.1506$	w$R = 0.1412$	w$R = 0.1402$

makes an angle of 2.31(9)° with the plane defined by the pyrazine ring C1C2N1N2C3C4, while the angle with the plane defined by the other pyrazine ring C5C6N3N4C7C8 is 4.30(9)°.

The two pyrazine rings of $Au(2)(pds)_2$ present a chair distortion in relation to the central plane defined by Au2Se5-Se6Se7Se8. This central plane makes an angle of 5.47(8)° with the plane defined by the pyrazine ring C9C10N5N6C11C12 and an angle of 8.68(9)° with the plane defined by the other pyrazine ring C13C14N7N8C15C16. The angle between the two planes defined by each one of the pyrazine rings is 4.99(9)°.

The $Au(1)(pds)_2$ and $Au(2)(pds)_2$ units are nearly coplanar, with a dihedral angle between their average planes of 4.62(3)° but with their longer axes aligned along nearly perpendicular directions (see Fig. 2).

Selected bond lengths and angles for the crystallographically independent $Au(1)(pds)_2$, $Au(2)(pds)_2$, ttf(1) and ttf(2) units are given in Tables 2 and 3, respectively. Table 2 shows that bond lengths and angles of the two independent $Au(pds)_2$ units are similar. There are several short distances (smaller than the sum of the van der Waals radii, S: 1.85 Å; Se: 2.0 Å[21]) that are listed in Table 4. These short contacts are established between Se atoms of $Au(2)(pds)_2$ and S atoms of ttf and between S atoms belonging to the two ttf(1) units within a dimer forming the network shown in Fig. 2b. There are no short contacts between ttf(1) and ttf(2) nor between $Au(1)(pds)_2$ and $Au(2)(pds)_2$. The distortions of the $Au(pds)_2$ from the expected ideal planar situation are certainly a consequence of these short interactions and other stereochemical crystal packing effects.

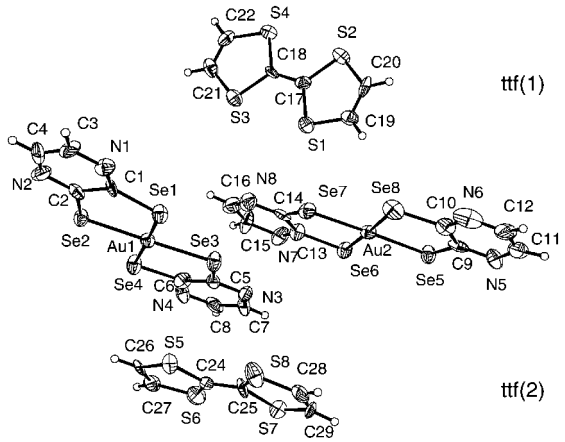

Fig. 1 ORTEP diagram and atomic numbering scheme of the ttf and of the $Au(pds)_2$ units in $(ttf)_2[Au(pds)_2]_2$ (**1**).

$(ttf)_3[Au(pds)_2]_2$, (2). This compound crystallises in the monoclinic system, space group $C2/m$, with the unit cell parameters given in Table 1. Fig. 3 shows the molecular numbering scheme for the $Au(pds)_2$ and the ttf units in this compound. The asymmetric unit contains half a ttf unit in the outer position of a trimer (ttf(1)), a quarter of the ttf unit in the center of the trimer (ttf(2)) and half of the $Au(pds)_2$ anion. Selected bond lengths and angles for the crystallographically independent $Au(pds)_2$, ttf(1) and ttf(2) units are given in Tables 5 and 6.

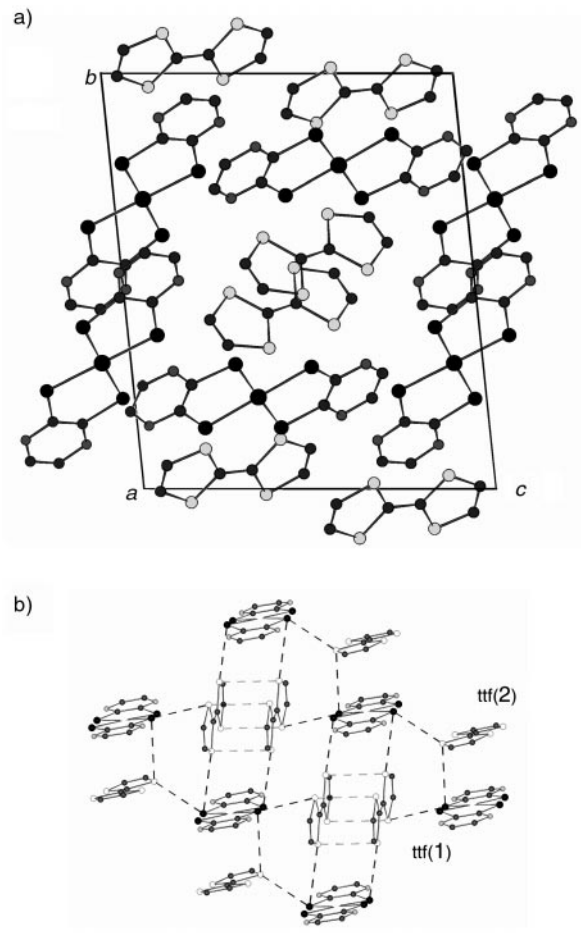

Fig. 2 Crystal structure of $(ttf)_2[Au(pds)_2]_2$ (**1**). a) View along (1,1,0). b) Network of short Se–S and S–S contacts between ttf(1), ttf(2) and $Au(2)(pds)_2$. $Au(1)(pds)_2$ was omitted for clarity.

Table 2 Selected bond lengths/Å and angles/° for the $Au(pds)_2$ units of $(ttf)_2[Au(pds)_2]_2$ (**1**)

$Au(1)(pds)_2$			
Au(1)–Se(4)	2.416(2)	Au(1)–Se(1)	2.420(2)
Au(1)–Se(2)	2.423(2)	Au(1)–Se(3)	2.434(3)
Se(4)–Au(1)–Se(1)	178.19(9)	Se(4)–Au(1)–Se(2)	86.83(8)
Se(1)–Au(1)–Se(2)	91.46(8)	Se(4)–Au(1)–Se(3)	91.53(8)
Se(1)–Au(1)–Se(3)	90.19(8)	Se(2)–Au(1)–Se(3)	177.63(9)
C(1)–Se(1)–Au(1)	101.5(6)	C(2)–Se(2)–Au(1)	102.2(7)
C(5)–Se(3)–Au(1)	100.9(6)	C(6)–Se(4)–Au(1)	101.6(7)
$Au(2)(pds)_2$			
Au(2)–Se(7)	2.419(3)	Au(2)–Se(5)	2.423(3)
Au(2)–Se(8)	2.425(3)	Au(2)–Se(6)	2.435(2)
Se(7)–Au(2)–Se(5)	178.25(9)	Se(7)–Au(2)–Se(8)	87.85(9)
Se(5)–Au(2)–Se(8)	91.33(9)	Se(7)–Au(2)–Se(6)	91.34(8)
Se(5)–Au(2)–Se(6)	89.55(8)	Se(8)–Au(2)–Se(6)	177.22(10)
C(9)–Se(5)–Au(2)	101.4(8)	C(13)–Se(6)–Au(2)	100.3(6)
C(14)–Se(7)–Au(2)	100.6(7)	C(10)–Se(8)–Au(2)	101.1(7)

Table 3 Selected bond lengths/Å for the ttf units of $(ttf)_2[Au(pds)_2]_2$ (**1**)

ttf(1)			
S(1)–C(19)	1.70(2)	S(1)–C(17)	1.74(2)
S(2)–C(20)	1.71(2)	S(2)–C(17)	1.71(2)
S(3)–C(21)	1.69(3)	S(3)–C(18)	1.702(19)
S(4)–C(22)	1.69(3)	S(4)–C(18)	1.71(2)
C(17)–C(18)	1.41(3)	C(19)–C(20)	1.29(3)
C(21)–C(22)	1.32(3)	S(5)–C(24)	1.69(2)
ttf(2)			
S(5)–C(26)	1.69(2)	S(6)–C(27)	1.66(3)
S(6)–C(24)	1.74(2)	S(7)–C(25)	1.72(2)
S(7)–C(29)	1.75(4)	S(8)–C(28)	1.70(3)
S(8)–C(25)	1.72(2)	C(24)–C(25)	1.37(3)
C(26)–C(27)	1.38(4)	C(28)–C(29)	1.28(5)

Table 4 Short contact distances/Å in $(ttf)_2[Au(pds)_2]_2$ (**1**)

Atoms	Distance/Å	*Symmetry operation
ttf(1) dimers		
S(1)–S(4)*	3.429(8)	$2-x,1-y,1-z$
S(2)–S(3)*	3.510(8)	$2-x,1-y,1-z$
Anion-cation contacts		
Se(7)–S(1)*	3.297(6)	x,y,z
Se(6)–S(4)*	3.604(6)	$2-x,1-y,1-z$
Se(8)–S(7)*	3.810(7)	$-x,1-y,-z$
Se(8)–S(3)*	3.840(6)	$1-x,1-y,1-z$
Se(6)–S(7)*	3.834(8)	$1-x,1-y,-z$

The crystal structure consists of trimerised stacks of ttf units along the *c* axis, separated by distorted $Au(pds)_2$ anions, which are almost perpendicular to the plane of the ttf units, as shown in Fig. 4. Within a trimer, the ttf units are related by an inversion center located at the central double C–C bond of the central ttf(2) unit. A preliminary report of this structure was given before.[6] It is now clear, in the final refinement of the structure, that there is no solvent (dichloromethane) inclusion in the structure, at variance with the previous report.[6] The positions previously attributed to solvent molecules (only the chlorine atoms) are now on the final refinement attributed to smaller residual electron density peaks.

The ttf units are almost planar, with rms deviations from their average plane of 0.040 Å in ttf(1) and 0.016 Å in ttf(2). The dihedral angle between the planes of ttf(1) and of ttf(2) is 0.2(1)°. The average plane of ttf(1) makes an angle of 77.45(4)° with the *c* axis. Within a trimer, the ttf units overlap with an eclipsed mode, at a distance of 3.54(1) Å. The closest distances between sulfur atoms of neighbouring ttf units within a trimer (S1···S3 = 3.502(5) and S2···S3 = 3.511(5) Å), are much smaller

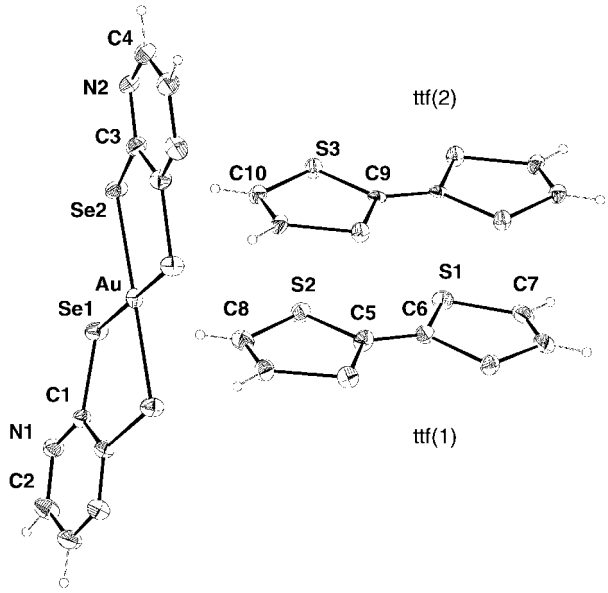

Fig. 3 ORTEP diagram and atomic numbering scheme of the ttf(1), ttf(2) and $Au(pds)_2$ units in $(ttf)_3[Au(pds)_2]_2$ (**2**).

Table 5 Selected bond lengths/Å and angles/° for the $Au(pds)_2$ unit of $(ttf)_3[Au(pds)_2]_2$(**2**)[a]

Au–Se(2)	2.4302(15)	Au–Se(2)#1	2.4302(15)
Au–Se(1)#1	2.4301(15)	Au–Se(1)	2.4301(15)
Se(2)–Au–Se(2)#1	90.76(7)	Se(2)–Au–Se(1)#1	179.50(6)
Se(2)#1–Au–Se(1)#1	89.57(5)	Se(2)–Au–Se(1)	89.57(5)
Se(2)#1–Au–Se(1)	179.50(6)	Se(1)#1–Au–Se(1)	90.10(7)
C(1)–Se(1)–Au	100.8(3)	C(3)–Se(2)–Au	102.4(4)

[a]Symmetry operation: #1 $x,-y,z$.

Table 6 Selected bond lengths/Å for the ttf units of $(ttf)_3[Au(pds)_2]_2$(**2**)[a]

ttf(1)			
C(5)–C(6)	1.41(2)	C(5)–S(2)#1	1.708(10)
C(5)–S(2)	1.708(10)	C(6)–S(1)	1.746(10)
C(6)–S(1)#1	1.746(10)	S(1)–C(7)	1.750(13)
C(7)–C(7)#1	1.31(3)	S(2)–C(8)	1.792(13)
C(8)–C(8)#1	1.32(3)		
ttf(2)			
S(3)–C(9)	1.714(8)	S(3)–C(10)	1.737(11)
C(9)–C(9)#2	1.41(3)	C(9)–S(3)#1	1.714(8)
C(10)–C(10)#1	1.34(2)		

[a]Symmetry operations: #1 $x,-y,z$ #2 $-x+1,-y,-z+1$.

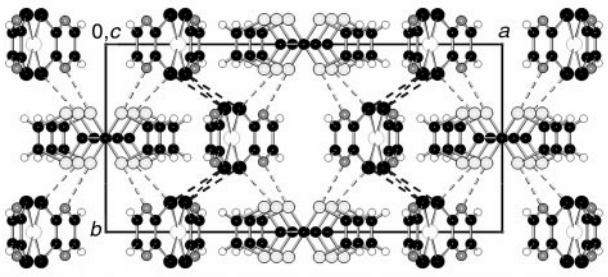

Fig. 4 Crystal structure of $(ttf)_3[Au(pds)_2]_2$ (**2**); viewed along the *b* axis.

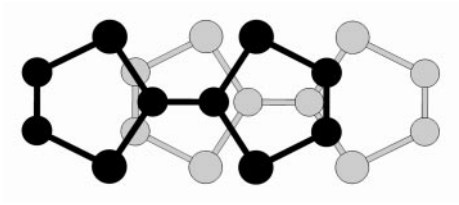

Fig. 5 Overlap mode between the ttf units of adjacent trimers of $(ttf)_3[Au(pds)_2]_2$ (**2**).

Table 7 Short contact distances/Å in $(ttf)_3[Au(pds)_2]_2$ (**2**)

Atoms	Distance	*Symmetry operation
Se(1)–Se(2)*	3.818(2)	$0.5-x,0.5-y,1-z$
Se(2)–Se(2)*	3.760(2)	$0.5-x,0.5-y,1-z$
Se(1)–S(3)*	3.702(4)	$0.5-x,0.5-y,1-z$
S(1)–N(1)*	3.102(12)	$0.5+x,0.5-y,z$
S(1)–S(3)*	3.502(5)	$1-x,y,1-z$
S(2)–S(3)*	3.511(5)	x,y,z

than the sum of the van der Waals radii (3.70 Å), thus denoting a strong interaction.

The contact between ttf units of different trimers is made by an overlap of the molecules slipped along their longer axis, as shown in Fig. 5, with an interplanar distance of 3.51(1) Å. This distance is shorter than the interplanar distance of the ttf units within a trimer. However the interaction energy, calculated using the extended Hückel method, between ttf units within a trimer is $\beta = 548.1$ meV, which is higher than that between ttf units of adjacent trimers, $\beta = 109.9$ meV. This is explained by the stronger interaction resulting from an eclipsed overlap mode, allowing for both π interaction (of the double C=C bonds) and sulfur–sulfur interaction. The staggered overlap of ttf units from adjacent trimers (see Fig. 5) allows for sulfur-π interactions which are not as strong, despite the shorter distance between the interacting units, as previously shown by Mori *et al.*[22]

The $Au(pds)_2$-anion complexes are not planar (Fig. 4), but have a significant boat distortion. The angles between the plane of the two pyrazine rings defined by C1N1C2 and by C3N2C4 and the central AuSe1Se2 plane are 13.7(5)° and 3.0(3)°, respectively. The average plane of the $Au(pds)_2$ complex makes an angle of 84.3(2)° with the average plane of ttf(1) and of 84.7(2)° with that of ttf(2).

Table 7 lists several short distances in the crystal. Among these we should mention the distance between selenium atoms of neighbouring $Au(pds)_2$ units, Se2–Se2* = 3.76(2) Å, which is much shorter than the sum of the van der Waals radii, 4.00 Å. It is also worth noting that the short distance between N1* and S1 may be, in addition to the previously mentioned contacts, responsible for the larger deviation of the pyrazine ring C1N1C2 in relation to the average plane through AuSe1Se2.

$(ttf)_3[Au(pds)_2]_3$, (3). This compound crystallises in the monoclinic system, space group $P2_1/n$, with the unit cell

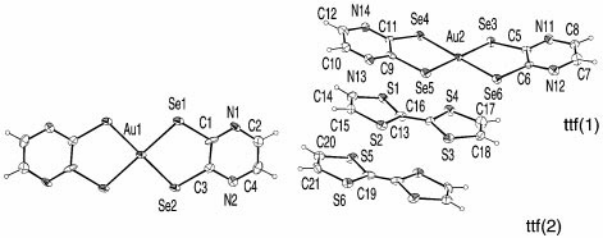

Fig. 6 ORTEP diagram and atomic numbering scheme of the ttf and of the $Au(pds)_2$ units in $(ttf)_3[Au(pds)_2]_3$ (**3**).

Table 8 Selected bond lengths/Å and angles/° for the $Au(pds)_2$ units of $(ttf)_3[Au(pds)_2]_3$(**3**)[a]

$Au(1)(pds)_2$			
Au(1)–Se(2)#1	2.427(2)	Au(1)–Se(2)	2.427(2)
Au(1)–Se(1)	2.431(2)	Au(1)–Se(1)#1	2.431(2)
Se(2)#1–Au(1)–Se(2)	180.0	Se(2)#1–Au(1)–Se(1)	88.61(7)
Se(2)–Au(1)–Se(1)	91.39(7)	Se(2)#1–Au(1)–Se(1)#1	91.39(7)
Se(2)–Au(1)–Se(1)#1	88.61(7)	Se(1)–Au(1)–Se(1)#1	180.0
C(1)–Se(1)–Au(1)	102.1(8)	C(3)–Se(2)–Au(1)	100.8(6)
$Au(2)(pds)_2$			
Au(2)–Se(3)	2.425(2)	Au(2)–Se(5)	2.426(2)
Au(2)–Se(4)	2.431(2)	Au(2)–Se(6)	2.433(2)
Se(3)–Au(2)–Se(5)	179.36(8)	Se(3)–Au(2)–Se(4)	88.73(7)
Se(5)–Au(2)–Se(4)	90.95(7)	Se(3)–Au(2)–Se(6)	90.93(7)
Se(5)–Au(2)–Se(6)	89.39(7)	Se(4)–Au(2)–Se(6)	179.57(7)
C(5)–Se(3)–Au(2)	100.9(5)	C(11)–Se(4)–Au(2)	102.2(5)
C(9)–Se(5)–Au(2)	102.0(5)	C(6)–Se(6)–Au(2)	101.7(5)

[a]Symmetry operations: #1 $-x,-y,-z$.

Table 9 Selected bond lengths/Å of the ttf units of $(ttf)_3[Au(pds)_2]_3$(**3**)[a]

ttf(1)			
C(13)–C(16)	1.39(3)	C(13)–S(1)	1.689(17)
C(13)–S(2)	1.74(2)	S(1)–C(14)	1.70(2)
S(2)–C(15)	1.73(2)	C(14)–C(15)	1.33(3)
C(16)–S(4)	1.693(19)	C(16)–S(3)	1.729(17)
S(3)–C(18)	1.70(2)	S(4)–C(17)	1.71(3)
C(17)–C(18)	1.32(3)		
ttf(2)			
C(19)–C(19)#2	1.36(5)	C(19)–S(5)	1.69(2)
C(19)–S(6)	1.76(2)	S(5)–C(20)	1.72(2)
S(6)–C(21)	1.74(2)	C(20)–C(21)	1.30(3)

[a]Symmetry operations: #2 $-x,-y+1,-z+1$.

parameters given in Table 1. In the unit cell there are two crystallographically independent ttf units and two $Au(pds)_2$ units. The asymmetric unit contains one and a half of each unit, $Au(pds)_2$ and ttf. Fig. 6 shows the molecular numbering scheme for $Au(pds)_2$ and ttf units. The gold atom Au(1) is at the centre of symmetry (0,0,0). The $Au(1)(pds)_2$ unit is nearly planar, with a rms deviation from the average plane of 0.016 Å. $Au(2)(pds)_2$ presents a boat distortion. The dihedral angles between the planes defined by the two pyrazine rings C5C6N12C7C8N11 and C9N13C10C12N14C11 and the plane defined by Au2Se3Se4Se5Se6 are 12.8(6)° and 6.7(8)°, respectively. Bond lengths and angles for the two independent $Au(pds)_2$ units are shown in Table 8. The ttf units are nearly planar with rms deviations from the least-squares best plane of 0.065 Å for ttf(1) and of 0.022 Å for ttf(2). Selected bond lengths of the ttf units are given in Table 9.

Fig. 7 shows a projection of the crystalline structure of $(ttf)_3[Au(pds)_2]_3$ (**3**) along the *a* axis. The ttf units are grouped in trimers, inside cages defined by four $Au(pds)_2$ units. The planar $Au(1)(pds)_2$ units lie parallel to the *b*, *c* plane, nearly perpendicular to the ttf units. The average plane of $Au(1)(pds)_2$ makes a dihedral angle of 86.4 (2)° with the plane of ttf(1), and angles of 88.1(3)° and 83.0(2)° with the planes of ttf(2) and $Au(2)(pds)_2$, respectively.

The staggered overlap mode of the ttf units within a trimer is shown in Fig. 8. There is an inversion center on the central C=C double bond of ttf(2). The ttf(1) and ttf(2) units are nearly coplanar and parallel with a dihedral angle of 1.7(4)°. The distance between the average planes of ttf(1) and ttf(2) is 3.50(4) Å. Table 10 lists several shorts contacts found in the $(ttf)_3[Au(pds)_2]_3$ (**3**) structure. Among these we should mention the short S···S contacts within a ttf trimer (S1–S5 = 3.567(9) Å, S2–S6 = 3.532(8) Å, S3–S5 = 3.554(8) Å and S4–S6 = 3.631(8) Å) which are shorter than the sum of the van der Waals radii (3.70 Å).

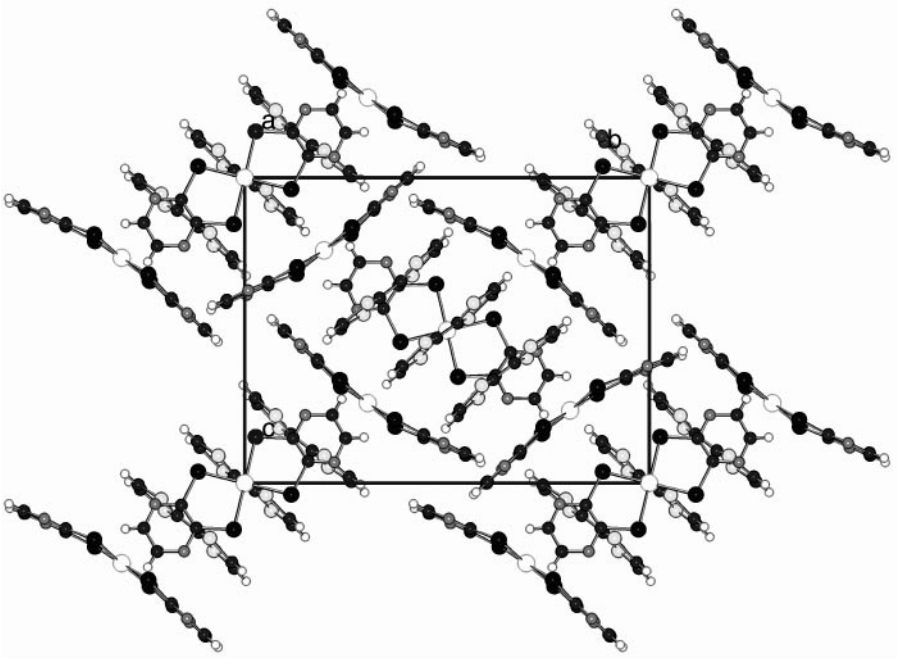

Fig. 7 Projection of $(ttf)_3[Au(pds)_2]_3$ (**3**) crystal structure in the *b*, *c* plane. The hydrogen atoms are omitted.

3.2. Analysis of the ttf overlap modes

The electrical transport properties of these ttf-based salts are expected to be determined by the ttf-based network, as will be discussed below. For most radical-cation salts, the existence of extended states, able to support electronic band-like mobility, derives from segregated regular stacks of the donor units or any extended network of close contacts, with π-overlap, between molecules.[5,23] For this reason we have paid close attention to the structural aspects of the ttf arrangements within these three compounds, in relation to the overall structure of the compounds and also with respect to their electrical and magnetic properties.

In these three salts, we have face-to-face interaction, or overlap, in the ttf dimers of compound **1** and in the trimers of compounds **2** and **3**, as described above. In this section we pay close attention to the different overlap mode of the ttf units in these trimers: eclipsed in **2** and staggered in **3**.

The eclipsed overlap mode of the ttf molecules within a trimer allows a strong interaction due to the close proximity of the sulfur atoms, as indicated by the calculations mentioned above. This overlap mode has been found in other ttf-based compounds, namely, $[ttf][Br]_{0.76}$,[24] $[ttf][I]_{0.71}$[25] and $[ttf][SCN]_{0.57}$,[26] these compounds have an eclipsed columnar structure, with interplanar distances between neighbouring ttf units of 3.572, 3.554 and 3.607 Å, respectively. These distances are slightly longer than the interplanar distance of 3.54(1) Å in the trimers of $(ttf)_3[Au(pds)_2]_2$ (**2**).

An eclipsed overlap was also reported for $(ttf)(ClO_4)$,[27] where the ttf units are grouped in dimers with an even shorter interplanar distance of 3.41 Å. This value is smaller than the interplanar distance found for the nearly eclipsed ttf dimers at 3.50(3) Å in $(ttf)_2[Au(pds)_2]_2$ (**1**). We mentioned above that the distance between ttf units of different trimers of $(ttf)_3[Au(pds)_2]_2$ (**2**) is shorter than the distance between the ttf units within a trimer. We showed by calculations that in view of the staggered overlap in the first case (inter-trimers) we have a smaller interaction between the ttf units.

A staggered overlap of the ttf units was previously found in (ttf)(tcnq)[28] and $(ttf)(I_3)$.[29] In the first case the ttf units form segregated columnar structures while in the second they are grouped in isolated $(ttf)_2^{2+}$ dimers. The ttf interplanar distances are 3.473(2) and 3.40(1) Å, respectively. These distances are comparable to the value of 3.50(4) Å for **3**.

We have carried out band structure calculations for **2**, as this is the only compound where the ttf units form segregated stacks, though they are trimerised. Only the HOMO (highest occupied molecular orbital) of ttf is assumed to be involved in the charge transfer and in the electronic interactions between the ttf species within the solids, as its energy separation from the two closest molecular orbitals (SHOMO and LUMO, *i.e.*, second highest occupied and lowest unoccupied molecular orbitals, respectively) is large (>2 eV). The band structure for these ttf stacks, calculated from the combination of the ttf's HOMO, consists of three bands, the first two being completely filled as imposed by the stoichiometry and discussed further

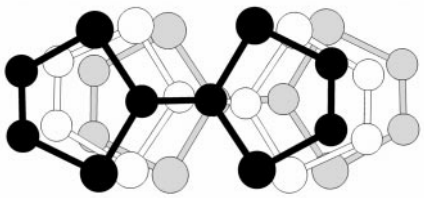

Fig. 8 Overlap mode of the ttf units within a trimer of $(ttf)_3[Au(pds)_2]_3$ (**3**).

Table 10 Short contact distances/Å in $(ttf)_3[Au(pds)_2]_3$ (**3**)

Atoms	Distance	Atoms	Distance	Atoms	Distance
Au(1)–S(5)[a]	3.348(5)	Au(1)–S(5)[b]	3.348(5)	Se(1)–Au(2)[c]	3.497(2)
Se(1)–S(5)[b]	3.599(6)	Se(1)–S(6)[d]	3.843(5)	Se(2)–S(1)[a]	3.597(6)
Au(2)–S(3)[e]	3.881(5)	Au(2)–S(4)[e]	3.907(6)	Se(4)–S(1)[e]	3.750(6)
Se(5)–S(2)[e]	3.718(7)	Se(5)–S(4)[f]	3.847(6)	Se(6)–S(6)[g]	3.745(5)
S(1)–S(5)[e]	3.567(9)	S(2)–N(12)[h]	3.434(19)	S(2)–S(6)[e]	3.532(8)
S(3)–N(1)[h]	3.45(1)	S(3)–S(5)[i]	3.554(8)	S(4)–N(1)[j]	3.572(17)
S(4)–S(6)[i]	3.631(8)				

[a]Symmetry operations: $0.5-x,-0.5+y,0.5-z$. [b]$-0.5+x,0.5-y,-0.5+z$. [c]$-x,1-y,-z$. [d]$0.5+x,0.5-y,-0.5+z$. [e]x,y,z. [f]$-0.5+x,1.5-y,-0.5+z$; [g]$-0.5-x,0.5+y,0.5-z$. [h]$-0.5-x,-0.5+y,0.5-z$; [i]$-x,1-y,1-z$; [j]$0.5-x,0.5+y,0.5-z$.

below. The energy gap between these conduction and valence bands, 2Δ, is estimated from these calculations to be ≈ 0.34 eV.

3.3. Charge distribution in the ttf units

EPR data for the three compounds, to be discussed below, indicates that the Au complex is a silent species as expected for the diamagnetic Au(III)$(pds)_2^-$ species. This is also consistent with the paramagnetic susceptibility data. The oxidation states of the ttf species can be estimated if neutrality for each solid is assumed, and we can formulate the three compounds, in terms of formal oxidation states, as $(ttf^+)_2[Au(pds)_2^-]_2$ (**1**), $[(ttf)_3]^{2+}[Au(pds)_2^-]_2$ (**2**) and $(ttf^+)_3[Au(pds)_2^-]_3$ (**3**). Thus, compounds **1** and **3** are fully ionic, and in compound **2** the ttf units are partially oxidised. We note that the fully ionic compounds **1** and **3** were obtained in acetonitrile while compound **2** was obtained by electrocrystallisation in the less polar solvent dichloromethane. The increase of the solvent polarity helps to stabilize the positive charge on ttf, facilitating the formation of the fully ionic composition.

The different atomic contributions to the HOMO of ttf, as shown in Fig. 9a, predict that the bond distances in ttf can be sensitive to the oxidation state, particularly the central C=C bond (**a**) and the C–S bond (**b**) lengths where C is the atom involved in the central double bond with the larger electron population. The variations of these bond lengths have been analysed in various reports[26,27,30] but its experimental verification requires quite accurate crystallographic data, usually obtained at low temperature.

Our data is not accurate enough to compare the C=C (**a**) and C–S (**b**) ttf bond lengths for the three compounds **1**, **2** and **3** (see Tables 3, 6 and 9).

To rationalise the charge distribution within the ttf trimers of $(ttf)_3[Au(pds)_2]_2$ (**2**) and $(ttf)_3[Au(pds)_2]_3$ (**3**), we have analysed

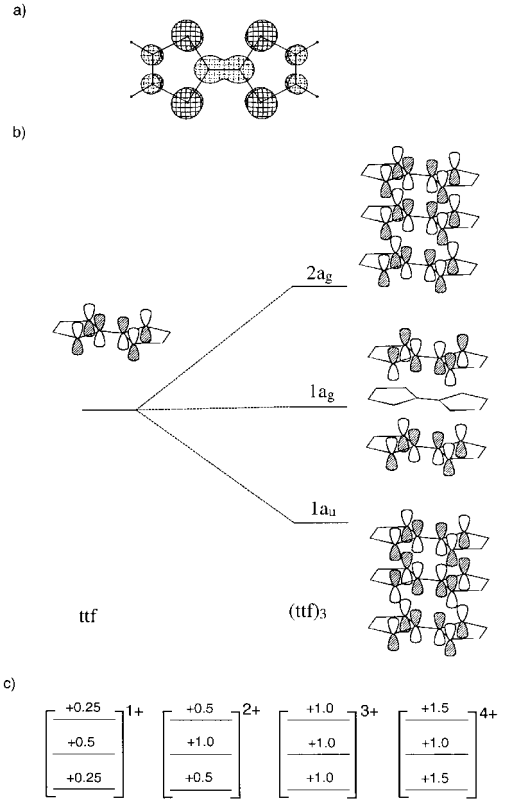

Fig. 9 a) HOMO of a ttf molecule, showing the contribution of the various atoms; b) Simplified diagram of the frontier orbitals of a model ttf trimer, obtained by combination of the HOMO; c) Charge distribution among the individual ttf units of a $(ttf)_3^{n+}$ model trimer, with n ranging from 1 to 4.

a model ttf trimer, formed by an eclipsed stacking of planar ttf units at an interplanar distance of 3.55 Å. The following bond distances (Å) were used: C–C 1.35, C–S 1.73, C–H 1.08. The characteristics of the trimer orbitals, resulting from the combination of the HOMO of the ttf units, are depicted in Fig. 9b. The energy separation is small (about 0.5 eV) since the distances between the adjacent ttf units is relatively long, giving rise to weak interactions. As shown in Fig. 9b, the lowest ($1a_u$) and the highest ($2a_g$) orbitals have contributions from the three ttf units, and have bonding and anti-bonding character, respectively. The middle orbital, $1a_g$, has non-bonding character and has contributions from the outer ttf units only. Fig. 9c shows the charge distribution for the individual ttf units of the model $(ttf)_3^{n+}$ trimer as a function of n, with n ranging from 1 to 4. This distribution is uneven except for $n=3$. The reason for this lies on the different contributions of the ttf units to each trimer orbital. For instance when going from $n=2$ to 3, the occupancy of the middle $1a_g$ orbital changes from double to single, and for $n=4$ it will be empty. As this $1a_g$ orbital has no contribution from the HOMO of the middle ttf unit, these changes on the charge of the trimer are only reflected on the formal charge localised in the outer ttf units. Accordingly, when n assumes the values 2, 3 or 4, the formal charge on the middle ttf unit remains $+1$, while the charges on each of the outer ttf units change from $+0.5$, to $+1.0$ and, finally, to $+1.5$. It should be pointed out that this result can be generalised to any other charge transfer solid with trimerised donors, since the same topology is expected for the trimer frontier orbitals.

In real solids, with extended networks of donor trimers, due to the structural characteristics of the solid, such as lack of symmetry, there may be a smoothing of the calculated charges on the individual molecules, and more dispersive (overlapping) bands. The possible effects resulting from the small interstack interaction were also neglected, but they are not expected to change the main results of the calculations.

From these calculations we would expect that in compound **2** the middle ttf unit of the trimer (ttf(2)) would have a formal charge closer to $+1$ and the outer ttf units (ttf(1) and ttf(1*)), would have a partial oxidation state close to $+0.5$. If this charge density is reflected in the bond lengths, as discussed above, the central C=C (**a**) and C–S (**b**) bonds of ttf(2) should be larger and shorter, respectively, than for ttf(1) (outer ttf unit of the trimer). In fact, despite the uncertainty of the calculations, a slight decrease of C–S (**b**) bond lengths is observed while the C=C (**a**) length remains unchanged. The higher density of positive charge in the middle ttf(2) unit of the trimer of compound **2** is expected to lead to stronger interactions with the neighbouring $Au(pds)_2$ anions, and this can explain the large number of short S···Se contacts between this unit and $Au(pds)_2$ (see Fig. 4).

In compound **3** the ttf units of the trimers are expected to have the same charge, and in fact the C=C (**a**) and C–S (**b**) bonds remain unchanged within experimental error (see Tables 6 and 9).

3.4. Electrical and magnetic properties

Compound 1 $(ttf)_2[Au(pds)_2]_2$. The electrical resistivity was measured in the temperature range 250–310 K by a d.c. method. The room temperature resistivity is 1×10^4 Ω cm, increasing upon cooling, with an activation energy $\Delta = E_g/2 = 0.245$ eV. The paramagnetic molar susceptibility, χ_p, was obtained from the magnetisation measurements, considering a diamagnetic contribution estimated from tabulated Pascal constants as $\chi_d = -5.70\times10^{-4}$ emu mol^{-1} and the results as a function of temperatures are shown in Fig. 10. At room temperature $\chi_p = 13.04\times10^{-4}$ emu mol^{-1} increasing, upon cooling, until about 45 K where it reaches a maximum value

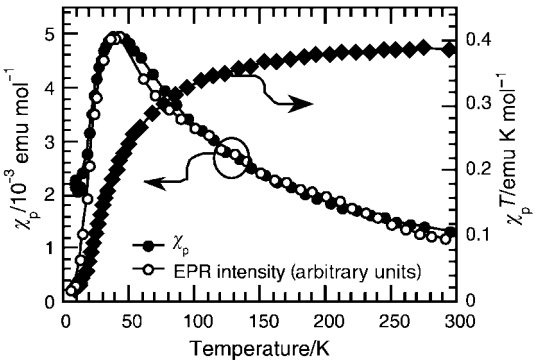

Fig. 10 Temperature dependence of the paramagnetic susceptibility, χ_p, of a polycrystalline sample (closed circles, left scale), EPR intensity for a single crystal (open circles, left scale), and $\chi_p T$ product (diamonds, right scale) of $(ttf)_2[Au(pds)_2]_2$ (**1**) as a function of temperature.

of 5.98×10^{-3} emu mol^{-1}. Upon further cooling below this temperature, the static susceptibility decreases until $\sim$12 K, where it starts to become dominated by the onset of a small Curie tail ascribed to impurities and defects.

EPR studies on single crystals showed a single Lorentzian line, with *g*-values typical of ttf with no indication of any Au complex contribution. These EPR results, indicate that the diamagnetic 3+ formal oxidation state of Au remains unchanged after combination with ttf. Therefore, we can formulate the compound as $(ttf^+)_2[Au(pds)_2^-]_2$. EPR anisotropy studies, at room temperature, on single crystals, are shown in Fig. 11. These results are consistent with only one orientation of the ttf^+ units giving rise to the EPR signal, such that their plane is nearly perpendicular to the longer crystal axis (needle-axis).

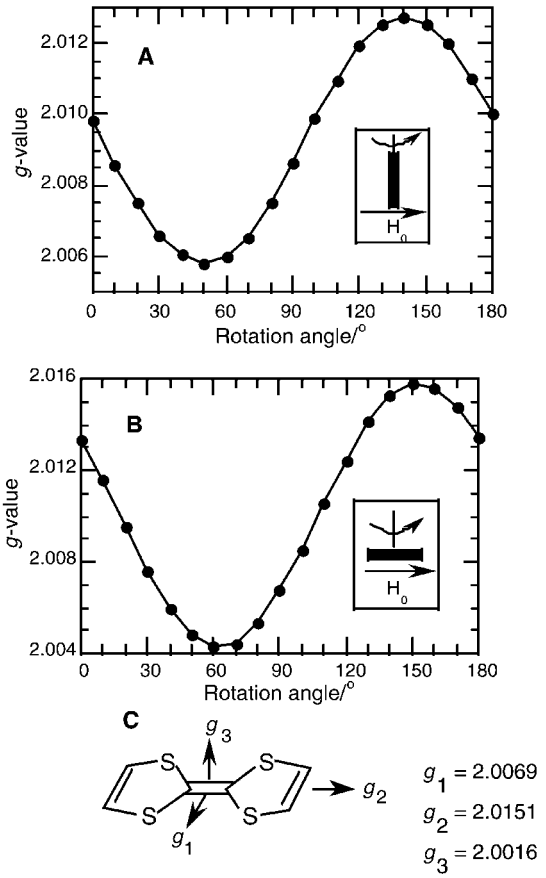

Fig. 11 (A and B) Anisotropy of the EPR *g*-value, at room temperature, for a single crystal of $(ttf)_2[Au(pds)_2]_2$ (**1**); (C) The principal *g*-values for ttf.

When the $(ttf)_2[Au(pds)_2]_2$ (**1**) crystal is rotated, at room temperature, keeping its longer needle-axis perpendicular to the static magnetic field, the *g*-value varies between 2.0058 and 2.0127. When the crystal is rotated so that the normal to the longer axis is kept perpendicular to the static magnetic field (the longer axis remains always horizontal to the static magnetic field) the *g*-value varies between 2.0043 and 2.0158. Comparing the anisotropy of the *g*-values with the reported principal *g*-values for ttf^+ ($g_1 = 2.0069$, $g_2 = 2.0151$ and $g_3 = 2.0016$)[31] we conclude that the ttf^+ units are likely to be oriented with their plane nearly perpendicular to the longer crystal axis. According to the crystal structure of $(ttf)_2[Au(pds)_2]_2$ (**1**) (Fig. 2), the planes of the two crystallographically independent ttf units, ttf(1) and ttf(2), make a dihedral angle of 77.12°. Therefore, these results strongly suggest that only one of these ttf units is responsible for the EPR signal and we propose that this is the isolated ttf(2) unit (see Fig. 2) The dimerised ttf(1) units, probably due to a strong antiferromagnetic coupling, are apparently EPR silent.

The temperature dependence of the EPR signal intensity in single crystals for different orientations, nearly follows the temperature dependence of the static paramagnetic susceptibility measured in a powder sample, with no traces of the small Curie tail seen in the powder sample (Fig. 10). In these samples we found no indication of the anisotropy of the EPR signal intensity previously reported.[6]

The static paramagnetic susceptibility in the high temperature range (above 100 K) can be well described by the Curie–Weiss law [see eqn. (1)]

$$\chi_P = C/(T - \Theta) \quad (1)$$

with $C = 0.421$ emu mol^{-1} K and $\Theta = -23.9$ K. This negative Θ denotes the presence of strong antiferromagnetic interactions as confirmed by the decrease of the $\chi_p T$ product upon cooling (Fig. 10). The Curie constant C is given by eqn. (2)

$$C = Ng^2 S(S+1)\mu_B^2/3k_B \quad (2)$$

where g is the Landé constant, μ_B is the Bohr magneton and k_B the Boltzmann constant. Considering the average g value for ttf as 2.008 and $S = \frac{1}{2}$, this Curie constant corresponds to $N = 6.71 \times 10^{23}$, which is slightly more than one spin per formula unit. Considering the molar formula $(ttf)_2[Au(pds)_2]_2$ (**1**), this result means that only $\approx$56% of the ttf^+ units contribute to the high temperature susceptibility, and is in agreement with the EPR data which shows a contribution from only one of the two ttf units. We therefore conclude that the paramagnetic susceptibility is dominated by the more isolated $ttf(2)^+$ species and probably, due to a strong antiferromagnetic coupling, the ttf(1) dimers have no significant contribution to the paramagnetic susceptibility.

After reaching a maximum at about 45 K, χ_p decreases to zero with decreasing temperature due to further antiferromagnetic interactions between the spins of the ttf(2) units. This decrease is more clearly observed in the EPR intensity of the single crystals, due a smaller contribution of impurity spins (Curie tail).

Compound 2 $(ttf)_3[Au(pds)_2]_2$. Electrical resistivity and thermopower measurements in this compound made along the needle axis, *c*, indicate a semiconducting behaviour (see Fig. 12). The electrical resistivity at room temperature is $\rho_{RT} \approx 100\ \Omega$ cm and increases upon cooling, with an activation energy $\Delta \approx 0.24$ eV. The thermopower at room temperature is large, $S \approx 750\ \mu V\ K^{-1}$, also increasing upon cooling confirming hole dominated thermally activated transport. This semiconducting behaviour agrees with the prediction from the band structure calculations. However the energy gap estimated from the electrical conductivity, 0.48 eV, is larger than the calculated

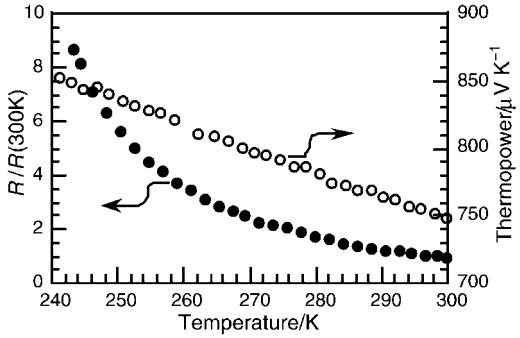

Fig. 12 Temperature dependence of the electrical resistivity (closed circles, left scale) and thermopower (open circles, right scale) of $(ttf)_3[Au(pds)_2]_2$ (**2**).

one (0.34 eV). This is not unexpected on the basis of the underlying approximations of the extended Hückel method. Similar differences have been reported for similar radical-cation salts.[32]

The paramagnetic susceptibility, χ_P, calculated from the magnetisation measurements with a diamagnetic contribution of 5.75×10^{-4} emu mol^{-1}, is very small at room temperature, in the order of 10^{-5} emu mol^{-1}, remaining nearly constant down to *ca.* 100 K. At lower temperatures it becomes dominated by a Curie tail ascribed to $\approx 3.4\%$ $S = \frac{1}{2}$ impurities, as shown in Fig. 13. This diamagnetic character is consistent with the band structure calculations. This compound presents a weak EPR signal in polycrystalline samples, characterised by the temperature independent *g*-values: $g_1 = 2.007$, $g_2 = 2.015$ and $g_3 = 2.002$, which are typical of ttf^+. The intensity of the EPR signal closely follows the temperature dependence of the paramagnetic susceptibility, as shown in Fig. 13, and it is ascribed to a small fraction of defects.

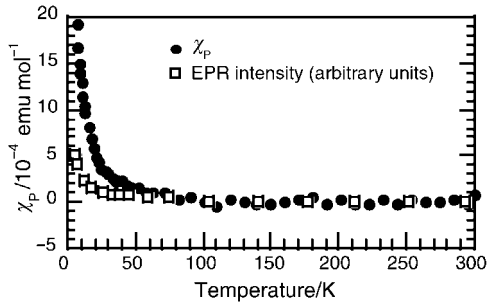

Fig. 13 Temperature dependence of the paramagnetic susceptibility, χ_P, (closed circles) and of the EPR signal intensity (open squares) for polycrystalline samples of $(ttf)_3$ $[Au(pds)_2]_2$ (**2**).

Compound 3, $(ttf)_3[Au(pds)_2]_3$. In view of the small dimensions of the crystals we could not measure the electrical resistance. The reduced amount of isolated material prevented static susceptibility measurements. EPR studies on a single-crystal showed a weak signal typical of ttf, with no significant temperature variation in the temperature range 100–300 K.

Conclusions

Depending on the preparation conditions three different compounds were obtained by combination of ttf and $Au(pds)_2$ anion: $(ttf)_2[Au(pds)_2]_2$ (**1**), $(ttf)_3[Au(pds)_2]_2$, (**2**), and $(ttf)_3[Au(pds)_2]_3$ (**3**). Fully ionic compounds **1** and **3**, with the same stoichiometry, were obtained in acetonitrile by interdiffusion and electrocrystallisation respectively. The preparation of partially oxidised compound **2** was possible in the less polar solvent dichloromethane. The higher electrical conductivity, although semiconducting, was found in **2**, where ttf units are partially oxidised and arranged in segregated stacks of trimers. These facts demonstrate that in order to obtain charge transfer salts with a desired structure it is not a simple choice of the donor–acceptor pair, in addition attention to the preparative conditions should be paid as well.

Acknowledgements

This work benefited from financial support from FCT, under contracts nr. PRAXIS/2/2.1/QUI/203/94 and POCTI/1999/CTM/35452.

References

1 (*a*) L. Alcácer and H. Novais, in *Extended Linear Chain Compounds*, ed. J. S. Miller, Vol. 3, Plenum Press, New York, 1983, ch. 6, 319; (*b*) M. Almeida and R. T. Henriques, in *Handbook of Organic Conductive Molecules and Polymers*, ed. Hari Singh Nalwa, John Wiley & Sons, Chichester, 1997, Vol. 1, p. 87; (*c*) P. Cassoux and L. Valade, in *Inorganic Materials*, ed. D. W. Bruce and D. O'Hare, Wiley, Chichester, 2nd ed., 1996, p. 1; (*d*) P. Cassoux and J. S. Miller, *Chemistry of Advanced Materials*, ed. L. V. Interrante and M. J. Hampden-Smith, Wiley-VCH, New York, 1998, p. 19.
2 (*a*) A. E. Underhill and M. M. Ahmad, *J. Chem. Soc., Chem. Commun.*, 1981, 67; (*b*) A. Braude, K. Carneiro, C. S. Jacobsen, K. Mortensen, D. J. Turner and A. E. Underhill, *Phys. Rev. B.*, 1987, **35**, 7835; (*c*) E. Underhill, P. I. Clemenson, M. B. Hursthouse, R. L. Short, G. J. Ashwell, I. M. Sandy and K. Carneiro, *Synth. Met.*, 1987, **19**, 953.
3 P. Cassoux, L. Valade, H. Kobayashi, A. Kobayashi, R. A. Clark and A. E. Underhill, *Coord. Chem. Rev.*, 1991, **110**, 115.
4 V. Gama, R. T. Henriques, G. Bonfait, M. Almeida, S. Ravy, J. P. Pouget and L. Alcácer, *Mol. Cryst. Liq. Cryst.*, 1993, **234**, 171.
5 J. M. Williams, J. R. Ferraro, R. J. Thorn, K. D. Carlson, U. Geiser, H. H. Wang, A. M. Kini and M.-H Whangbo, *Organic Superconductors, Including Fullerenes: Synthesis, Structure, Properties, and Theory*, Prentice-Hall, Englewood Cliffs, NJ, 1992.
6 J. Morgado, M. T. Duarte, L. Alcácer, I. C. Santos, R. T. Henriques and M. Almeida, *Synth. Met.*, 1997, **86**, 2187.
7 G. C. Papavassiliou, S. Y. Yiannopoulos and J. S. Zambounis, *Chem. Scr.*, 1987, **27**, 265.
8 F. Wudl, *J. Am. Chem. Soc.*, 1975, **97**, 1962.
9 CAD4 (Enraf-Nonius), CAD-4 software, Version 5.0, Enraf-Nonius, Delft, The Netherlands, 1989.
10 G. M. Sheldrick, SHELXS86, *Acta Crystallogr., Sect. A: Fundam. Crystallogr.*, 1990, **46**, 467.
11 G. M. Sheldrick, SHELXL97, A Program for Crystal Structure Refinement, University of Göttingen, Germany, 1997.
12 M. N. Burnett and C. K. Johnson, ORTEPIII. Report ORNL-6895, Oak Ridge National Laboratory, Tennessee, USA, 1996.
13 E. Keller, SCHAKAL-97, A Computer Program for the Representation of Molecular and Crystallographic Models, Kristallographisches Institut der Universität Freiburg i., Br., Germany, 1997.
14 (*a*) R. Hoffmann, *J. Chem. Phys.*, 1963, **39**, 1397; (*b*) R. Hoffmann and W. N. Lipscomb, *J. Chem. Phys.*, 1962, **36**, 2179.
15 J. H. Ammeter, H.-J. Bürgi, J. C. Thibeault and R. Hoffmann, *J. Am. Chem. Soc.*, 1978, **100**, 3686.
16 (*a*) M. H. Whangbo and R. Hoffmann, *J. Am. Chem. Soc.*, 1978, **100**, 6093; (*b*) M. H. Whangbo, W. M. Walsh, Jr., R. C. Haddon and F. Wudl, *Solid State Commun.*, 1982, **43**, 637; (*c*) M. H. Whangbo, J. M. Williams, M. A. Beno and J. R. Dorfman, *J. Am. Chem. Soc.*, 1983, **105**, 645.
17 C. Mealli and D. M. Proserpio, *J. Chem. Ed.*, 1990, **67**, 39.
18 E. B. Lopes, ITN, Internal Report, 1981.
19 P. M. Chaikin and J. F. Kwak, *Rev. Sci. Instrum.*, 1975, **46**, 218.
20 R. P. Huebner, *Phys. Rev.*, 1964, **135**, A1281.
21 L. Pauling, *The Nature of the Chemical Bond*, Cornell University Press, 3rd edn., 1967.
22 T. Mori, A. Kobayashi, Y. Sasaki, H. Kobayashi, G. Saito and H. Inokuchi, *Bull. Chem. Soc. Jpn.*, 1984, **57**, 627.
23 For a general overview see also *Lower Dimensional Solids and Molecular Electronics*, eds. R. M. Metzger, P. Day and G. Papavassiliou, 1991, Plenum Press.
24 S. J. La Placa, P. W. R. Corfield, R. Thomas and B. A. Scott, *Solid State Commun.*, 1975, **17**, 635.
25 C. K. Johnson and C. R. Watson, Jr., *J. Chem. Phys.*, 1976, **64**, 319.

26 H. Kobayashi and K. Kobayashi, *Bull. Chem. Soc. Jpn.*, 1977, **50**, 3127.
27 K. Yakushi, S. Nishimura, T. Sugano, H. Kuroda and I. Ikemoto, *Acta Crystallogr., Sect. B: Struct. Crystallogr. Cryst. Chem.*, 1980, **36**, 358.
28 (*a*) T. J. Kistenmacher, T. E. Phillips and D. O. Cowan, *Acta Crystallogr., Sect. B: Struct. Crystallogr. Cryst. Chem.*, 1974, **30**, 763; (*b*) A. J. Schultz, G. D. Stucky, R. H. Blessing and P. Coppens, *J. Am. Chem. Soc.*, 1976, **98**, 3194.
29 R. C. Teitelbaum, T. J. Marks and C. K. Johnson, *J. Am. Chem. Soc.*, 1980, **102**, 2986.
30 K. Kondo, G. Matsubayashi, T. Tanaka, H. Yoshioka and K. Nakatsu, *J. Chem. Soc., Dalton Trans.*, 1984, 379.
31 I. S. Jacobs, J. W. Bray, H. R. Hart Jr., L. V. Interrante, J. S. Kasper, G. D. Watkins, D. E. Prober and J. C. Bonner, *Phys. Rev. B*, 1976, **14**, 3036.
32 J. Morgado, I. C. Santos, L. F. Veiros, R. T. Henriques, M. T. Duarte, M. Almeida and L. Alcácer, *J. Mater. Chem.*, 1997, **7**, 2387.